Fly ash-$Ca(OH)_2$ reactivity in hypersaline NaCl and $CaCl_2$ brines

Marie Collin ([,†]), Dale P. Prentice ([*,†]), Ross Arnold ([*,†]), Kirk Ellison ([‡]), Dante Simonetti ([§,†]), Gaurav Sant ([*,†,**,††])*

ABSTRACT

The disposal of highly concentrated brines from coal power generation can be effectively accomplished by physical solidification and chemical stabilization (S&S) processes that utilize fly ashes as a reactant. Herein, pozzolanic fly ashes are typically combined with calcium-based additives to achieve S&S. While the reactions of fly ash-(cement)-water systems have been extensively studied, the reactivity of fly ashes in hypersaline brines (ionic strength, I_m > 1 mol/L) is comparatively less understood. Therefore, the interactions of a Class C (Ca-rich) and a Class F (Ca-poor) fly ash were examined in the presence of $Ca(OH)_2$, and their thermodynamic phase-equilibria modeled on contact with NaCl or $CaCl_2$ brines for $0 \leq I_m \leq 7.5$ mol/L. At low ionic strengths (< 0.3 mol/L), reactivity and stable phase-assemblages remain effectively unaltered. But, at high(er) ionic strengths (> 0.5 mol/L), the phase assemblage shows a particular abundance of Cl-AFm compounds (i.e., Kuzel's and Friedel's salt). Although Kuzel's and Friedel's salt formation enhances Class F fly ash reactions in both NaCl and $CaCl_2$ brines; NaCl brines compromise Class C fly ash reactivity substantially, while $CaCl_2$ results in the reactivity remaining essentially unchanged. Thermodynamic modeling that accounts for the fractional, and non-congruent dissolution of the fly ashes indicates that their differences in reaction behavior are provoked by differences in the prevalent pore solution pH, which affects phase stability. The outcomes offer new insights for matching fly ashes, Ca-additives, and brines, and accounting for, and controlling fly ash-brine interactions as relevant to optimizing physical solidification and chemical stabilization applications.

Keywords: Fly ash; Brine encapsulation; Solidification/stabilization; Thermodynamic modeling

INTRODUCTION AND BACKGROUND

As industrial sites face increasing challenges in managing wastewater, effective technologies for managing such reject streams are needed. A primary concern for many sites is finding a way to eliminate the discharge of wastewater as they work towards meeting zero-liquid discharge (ZLD) guidelines. One such wastewater is Flue Gas Desulfurization Wastewater (FGDWW) from coal-fired electricity generation which contains high levels of dissolved salts (0-5 mol/L of total dissolved solids),[1,2] including alkali cations, halide anions, and heavy metals. A potential

[*] Laboratory for the Chemistry of Construction Materials (LC^2), Department of Civil and Environmental Engineering, University of California, Los Angeles, CA, USA
[†] Institute for Carbon Management, University of California, Los Angeles, CA, USA
[‡] Electric Power Research Institute, Charlotte, NC 28262, USA
[§] Department of Chemical and Biomolecular Engineering, University of California, Los Angeles, CA, USA
[**] Department of Materials Science and Engineering, University of California, Los Angeles, CA, USA
[††] California Nanosystems Institute (CNSI), University of California, Los Angeles, CA, USA

Corresponding authors: M. Collin (mariecollin03@ucla.edu) and G. Sant (Email: gsant@ucla.edu)

solution to safely dispose of such wastewaters, as well as other chemically similar wastewaters (i.e, coal ash landfill leachate, contaminated groundwater, and produced water) is to encapsulate such wastewater in a solid matrix.[3,4] To reduce disposal volumes, wastewaters are often concentrated resulting in a hypersaline solution (i.e., referred to as a brine hereafter due to their high salt concentrations). In the encapsulation or S&S process, the solution reacts with a binder to form a cemented/cohesive monolith. This monolith retains the dissolved salts originally present in the brine.[3,4] Such salts may be entrapped by precipitation as insoluble species,[5] by sorption on the surfaces of hydrated phases,[6] and/or by incorporation into the lattice (structure) of the hydrated phases.[7,8] Furthermore, the solution may also be entrapped within the pore spaces of the solidified mass. Many cementitious binders have been examined to obtain a solid that can be safely landfilled.[9,10] In particular, there is considerable interest in the use of fly ashes; i.e., a co-product of coal combustion on account their ability to motivate so-called pozzolanic reactions upon reaction with water contained in the brine, in the presence of calcium-based additives including quick lime, hydrated lime, and/or ordinary Portland cement (OPC).[3,4,9] Recently, Song et al. suggested that typical ASTM classifications of fly ashes that are used to assess their use in construction applications (e.g., using ASTM C618) may have led to the exclusion of fly ashes whose reactivity was underestimated.[11] Lower-performance requirements (e.g., in terms of strength) of encapsulation materials would imply that a wide range of fly ashes, including current production and harvested and reclaimed ("historical production") fly ashes, may be suitable for use in S&S applications. This is important as the diminishing availability of high-quality fly ashes would not, in the short- to medium-term, affect the use/availability of fly ashes for brine encapsulation. This is significant because fly ashes, e.g., as compared to cement-based materials, provide a lower cost solution, and lower-carbon footprint solution, for S&S applications, wherein the use of cement-based materials is desirable as (minor) additives, but not as the dominant component of the binder composition.[12,13]

The performance of a binder for encapsulation applications is ascertained in terms of its ability to immobilize constituents that could potentially contaminate groundwater. The brine's composition (i.e., in the case of coal-power based electricity production) is often dominated by NaCl, $CaCl_2$ and/or $CaSO_4$; although solubility considerations ensure that, typically, the abundance of SO_4^{2-} is often far inferior to Cl^- anions. The presence of Cl^- at high concentrations can strongly affect the phase assemblage that forms in cementitious systems. For example, Cl^- species can physisorb onto the C-S-H phases,[14–16] and they can also occupy the interlayer positions in AFm phases (i.e. phases of the general formula $[Ca_2(Al,Fe)(OH)_6]\cdot X\cdot xH_2O$ with X = OH^-, SO_4^{2-},CO_3^{2-} and/or Cl^-) to form hydrocalumite ($Ca_2Al(OH)_{12}[Cl, CO_3,OH]_2\cdot 4H_2O$), Kuzel's salt ($Ca_2Al(OH)_6[Cl, SO_4, OH]\cdot 2H_2O$) or Friedel's salt ($Ca_2Al(OH)_6[Cl, OH]\cdot 2H_2O$) ["Cl-AFm phases" hereafter].[17–21] On the other hand, in lime-enriched systems, Cl^- species can additionally react with portlandite ($Ca(OH)_2$) to form calcium oxychloride compounds.[22–24]

Thermodynamic modeling based on the minimization of Gibbs free energy is a powerful tool for assessing stable phase equilibria and equilibrium compositions of the solid-, liquid (and gas)-phases as relevant to encapsulation applications. But, the current implementations of such modeling often rely on assumptions including: congruent dissolution of the fly ash,[9] and most often, an inability to incorporate the actual degree of fly ash reaction which could be

particularly affected in hypersaline environments that feature a reduced water activity.[25–30] For example, the dissolution rates of crystalline and amorphous materials could either enhance or decrease in hypersaline environments in relation to their composition, and concentration.[31–36] For example, seawater has been suggested to enhance the fly ash's pozzolanic reactions.[37] Since changes in reactivity alter not only the kinetics of reactions, but also the phase assemblage that forms, it is important to assess these aspects due to the obvious implications on contaminant retention by the solidified waste forms. With this focus in mind, this study examines the effect of NaCl or $CaCl_2$-based hypersaline brines on the pozzolanic reactions of Ca-rich (Class C) and Ca-poor (Class F) fly ashes. Special focus is paid to model, compare, and ascertain discrepancies between the results of thermodynamic modeling and experimental assessments of stable phase assemblages for mature systems (i.e., aged greater than 10 days at 50 °C). The outcomes provide new insights to understand how the composition of the brine affects the stable phase assemblage that forms thereby offering guidance to screen and select the most compatible combinations of fly ashes, and brines to ensure optimal wastewater encapsulation (i.e., physical solidification and chemical stabilization: S&S).

MATERIAL AND METHODS

Raw material characterization

A Class C and Class F fly ash were considered herein. Their bulk oxide compositions, which encompass both crystalline and amorphous compounds as determined using X-ray fluorescence (XRF), is shown in Table 1. The crystalline phases present, and the quantity of the amorphous phase present, were quantified using Quantitative X-Ray Diffraction (QXRD) and Rietveld refinement.[38,39] Zincite (ZnO, purity: 99.999%) was used as an internal standard at a mass loading of 10 mass % in the Rietveld refinement which was carried out using Profex.[40] The quantities and types of crystalline phases present is shown in Table 2. The average composition of the amorphous phase was calculated by subtracting the quantity of crystalline phases from the bulk XRF composition,[11] and is shown in Table 3.

Both fly ashes were subjected to 50 min of dissolution in dilute conditions (solid-to-liquid ratio, mass basis, s/l = 1:1000) in deionized water (DIW, Milli-Q: 18.2 MΩ/cm) at 50 °C under agitation in high density polyethylene (HDPE) containers. The residual solids were retrieved from the container after 50 minutes of dissolution by vacuum-filtration through a 11 µm paper filter, dried at 60 °C, and analyzed using XRD to determine which crystalline phases had dissolved. Based on this analysis, the crystalline phases were designated as: not soluble (NS), partially soluble (PS), or soluble (S). These are designations not so much of "solubility" per se, but rather describe the extent to which a compound may dissolve over the period of dissolution, i.e., either remaining undissolved, being partially dissolved, or fully dissolved (see Table 2).

Simulated brines were prepared by dissolving NaCl (99% purity) or $CaCl_2{\cdot}6H_2O$ (99% purity) in deionized water (DIW) at room temperature to obtain solutions with salt concentrations of 0, 0.01, 0.1, 0.5, 1, 2 ($CaCl_2$ and NaCl), 2.5 ($CaCl_2$ only) and 5 (NaCl only) mol/L. These concentrations translate to ionic strengths (I_m; mol/L) of 0.01, 0.1, 0.4, 1, 2, and 5 mol/L for the NaCl solution, and 0.03, 0.3, 1.5, 3, 6, 7.5 mol/L for the $CaCl_2$ solutions. Note that, for $CaCl_2$, the highest concentration used was 2.5 mol/L (I_m = 7.5 mol/L), as higher concentrations do not

allow the formulation of a fluid cementitious paste at the s/l studied. Cementitious formulations were composed by combining 55 mass % fly ash, 10 mass % portlandite ($Ca(OH)_2$; purity > 95%) and 35 mass % brine. The formulation was mixed for 45 s at 270 rpm and 1 min at 480 rpm at room temperature using a high-shear immersion mixer. The resulting pastes were rapidly poured into glass ampoules, hermetically sealed, and placed into a TamAir isothermal calorimeter at 50 °C for analysis of their heat release behavior. Heat flow and cumulative heat release were measured to assess the rate and the extent of fly ash reaction. A temperature of 50 °C was chosen as it is known to be sufficient to accelerate fly ash reactions[‡‡].[41,43] In general, the heat release showed little if any change ($d\dot{Q}/dt$ < 0.1 mW/g/s) after 10 days (see Figure S1), following which the ampoules were extracted, and the samples crushed and immersed in isopropanol (IPA), to induce solvent-exchange, for 1 week to cease reactions.[44] Thereafter, the samples were dried under vacuum for another week, following which they were crushed, milled using an agate mortar and pestle and then sieved through a 300 µm sieve prior to any additional characterization.

Table 1. The bulk (total oxide) composition of the Class C and Class F fly ashes as determined using XRF using a fusion method (ASTM D4326).[45]

	Amount (mass %)	
	Class C	**Class F**
CaO	28.0	4.0
MgO	7.2	0.9
Al_2O_3	18.5	20.7
SiO_2	32.1	52.0
SO_3	3.0	0.8
Fe_2O_3	5.3	14.6
Na_2O	1.8	1.4
K_2O	0.4	2.4
Others	3.7	3.2
Total	100.0	100.0

Table 2. The crystalline phases present in the fly ashes as determined using QXRD (mass %). Here, ^{NS} indicates the phases that were determined to be not-soluble, ^{PS} indicate the phases that are partially soluble with the percentage dissolved recorded in brackets, and ^{S} indicates the phases that are completely dissolved after 50 minutes of fly ash dissolution in dilute conditions (s/l = 1:1000).

	Class C	**Class F**
Quartz – SiO_2	5.0 ^{NS}	6.0 ^{NS}
Periclase – MgO	3.3 ^{NS}	-
Free lime – CaO	1.4 ^{S}	0.4 ^{S}
Anhydrite – $CaSO_4$	1.7 ^{S}	0.6 ^{S}

[‡‡] Assuming an apparent activation energy of the pozzolanic fly ash reactions to be on the order of 50 kJ/mol[41,42] implies that curing at 50 °C for 10 days equates to around 50 days of curing at ambient conditions (25 °C).

Tricalcium aluminate – $Ca_3Al_2O_6$	3.3 PS (30%)	-
Merwinite – $Ca_3Mg[SiO_4]_2$	1.7 PS (39%)	-
Magnetite – Fe_3O_4	-	2.1 NS
Maghemite – γ-Fe_2O_3	-	0.9 NS
Hematite – α-Fe_2O_3	-	0.9 NS
Gehlenite – $Ca_2Al[AlSiO_7]$	0.8 NS	-
Magnesite – $MgCO_3$	0.5 NS	-
Portlandite – $CaOH_2$	~0.4 (TGA) S	~0.7 (TGA) S
Ye'elimite – $Ca_4Al_6O_{12}SO_4$	0.5 S	-
Mullite – $3Al_2O_32SiO_2$	0.8 NS	5.2 NS
Quantity of crystalline phases (mass %)	19.4	16.8
Amorphous content (mass %)	80.6	83.2

Table 3. The average composition of the amorphous component as calculated by subtracting the crystalline content from the bulk XRF (total oxide) composition.

	Amount (mass %)	
	Class C	**Class F**
CaO	22.1	2.6
MgO	3.5	0.9
Al_2O_3	16.1	17.9
SiO_2	26.2	45.9
SO_3	1.9	0.5
Fe_2O_3	5.2	10.7
Na_2O	1.8	1.3
K_2O	0.4	2.3
Others	3.2	1.2
Total	80.4	83.3

Material characterization

Thermogravimetric analysis: Thermogravimetric analysis (TGA) was performed using a Perkin Elmer STA 6000 under a flow of ultra-high purity (UHP) N_2 in aluminum oxide crucibles. A heating rate of 10 °C min^{-1} was used between 35 and 950 °C, after 5 min equilibration at 35 °C. The mass loss (TG) and the derivative mass loss (DTG) were used to characterize and quantify several hydrate phases, including portlandite, Cl-AFm, etc.[46] The analysis was performed on powdered samples that had undergone solvent exchange using IPA. While this prevents quantification of the free water content, it does not affect the remainder of the solid phase-specific mass determinations.[46]

Quantitative information regarding the Cl-AFm phases, i.e., Friedel's salt and Kuzel's salt, can be obtained using TGA.[18,46,47] These hydrates display two significant mass losses in the temperature range of ~100-180 °C and ~180-450 °C. The first mass loss is attributed to interlayer water removal, while the second results from removal of the main-layer water.[46] In our system, the first mass loss occurred coincidentally with that of water removal from C-S-H,

ettringite and/or monosulfoaluminate. Consequently, this peak could not be used for Cl-AFm quantification. The second mass loss, however, occurs in a temperature range where no water removal from the other phases is observed. But, since the mass loss of Friedel's salt and Kuzel's are superimposed with each other, independent quantifications of each phase was not possible herein. Nevertheless, comparing the mass loss measured between ≈250-to-430 °C helps to assess the total quantity of Cl-AFm phases formed in each system.

Infrared spectroscopy: Solid-state attenuated total reflection Fourier-transform infrared spectroscopy (ATR-FTIR) was performed using a Spectrum Two FT-IR Spectrometer (Perkin Elmer). The powdered samples were pressed using around 90 N of force onto a diamond/ZnSe composite crystal to ensure good contact and generate total internal reflection. The spectra reported herein were obtained by averaging 4 scans over the wavenumber range of 4000-to-400 cm^{-1} at a resolution of 1 cm^{-1}.

X-Ray diffraction: XRD analysis was performed using a PANalytical X'PertPro diffractometer (θ-θ configuration, Cu-Kα radiation, α = 1.54 Å) on powdered samples. The scans were acquired using a rotating sample stage between 5° and 70° with a step size of 0.02° using a X'Celerator 2 detector. In general, powdered samples were placed in the sample holder and their surfaces gently textured to minimize the potential for preferred orientation related errors.

Thermodynamic modeling: Thermodynamic modeling was carried out using GEM-Selektor v.3.6 (GEMS)[48,49] which incorporates the slop98.dat and Cemdata18 thermodynamic databases.[50–54] To represent the non-ideality of the solutions, the activity coefficients were calculated using the Truesdell-Jones extension to the Debye-Hückel equation that is applicable for I_m ≈ 2 mol/L:[55]

$$\log_{10}\gamma_i = \frac{-A_\gamma z_i^2\sqrt{I}}{1+\ \dot{a}B_\gamma\sqrt{I}} + \ b_\gamma I + \log_{10}\frac{X_{jw}}{X_w} \qquad \text{Equation (1)}$$

where, γ_i is the activity coefficient and z_i the charge of the ith aqueous species, A_γ and B_γ are temperature and pressure dependent coefficients, X_{jw} is the molar quantity of water, X_w is the total molar amount of the aqueous phase, and I is the molal ionic strength. A common ion size parameter ($a = 3.72$ Å) and a short-range interaction parameter ($b_\gamma = 0.64$ kg/mol) were used, treating NaCl as the background electrolyte.[55,56] Water activity is generally defined as the deviation of the chemical potential of liquid water from its pure state (where water activity = 1) to a 'non-pure' state (where water activity < 1) due to the presence of a solute. To a first approximation, water activity in GEMS is calculated from the osmotic coefficient when the extended Debye-Hückel activity model for aqueous species is used, following Helgeson et al.:[48,55]

$$\ln a_{water} = -\frac{\phi\, m_\Sigma}{55.508435} \qquad \text{Equation (2)}$$

where, m_Σ is the sum of all species molalities and ϕ is the osmotic coefficient, both of which are calculated within GEMS as following Helgeson et al.[55]

The system modelled (55 g of FA, 10 g of portlandite, and 35 g of brine) is equivalent to that studied experimentally. Here, brine concentrations of 0, 0.01, 0.1, 0.5, 1, and 2 (NaCl only) mol/L and up to 1 mol/L of $CaCl_2$ were considered to conform to the limits of applicability of Equation (1). Of course, as water is consumed over the course of reaction, the ionic strength exceeds the 2 mol/L limit. Although GEMS offers an option to use Pitzer's model which can accurately describe ion activities in highly-concentrated solutions (I_m < 6 mol/L),[57] this module was not used due to a lack of ion-specific parameters to consider all the species that are present herein. Nonetheless, it should be noted that previous comparisons of ion activities determined using Pitzer's equations and the parameterization of the Truesdell-Jones ion-activity model for simple Ca, Na, and Cl containing systems yield results within ±30% for I_m < 4 mol/L.[9,57,58] Given that I_m < 3.5 mol/L for all solution compositions considered herein, while the absolute quantitative accuracy of the predictions of phase equilibria would degrade for I_m > 2 mol/L, qualitative indicators (e.g., the types, and relative abundance of phases formed) would nevertheless continue to be relevant to the systems studied. As such, some uncertainty is expected in the quantitative (although not qualitative) outcomes of the simulations performed at higher ionic strength.[48,58] In general, portlandite is considered to be fully consumed over the course of reactions, while the fly ashes are considered to show fractional reactivity based on: (a) the near-inert nature of the insoluble crystalline phases (e.g., quartz), (b) incomplete reaction of some partially soluble crystalline phases, (c) complete consumption of the highly-reactive crystalline phases (e.g., $CaSO_4$), and (d) the congruent dissolution of the amorphous phase in accordance with its average composition (Table 3).

RESULTS AND DISCUSSION

Hydrate formation: The formation of crystalline and amorphous reaction products was examined in the Class C and Class F fly ashes after 10 days of reaction at 50 °C. Among the crystalline phases, ettringite (PDF #04-013-3691), monosulfoaluminate (AMCSD #0014757), a magnesium-aluminum hydrotalcite-like phase (referred to as 'hydrotalcite' hereafter, PDF #00-014-0525), katoite (AMCSD #0006980), Kuzel's salt (PDF #00-019-0203), Friedel's salt (AMCSD #0014832), and strätlingite (AMCSD #0006404) were observed. Expectedly, the phase assemblages formed differ considerably across Class C and Class F fly ashes (see Figure 1). For example, upon reaction in DI-water, the Class F fly ash system shows the presence of ettringite (identified by its main peak at 9.08° 2θ), which in time, transforms into monosulfoaluminate (9.93° 2θ). In contrast, the Class C fly ash shows the presence of monosulfoaluminate, katoite (32.61° 2θ), hydrotalcite (11.63° 2θ) and traces of strätlingite (7.00° 2θ). The introduction of low concentrations of NaCl or $CaCl_2$ (I_m < 0.3 mol/L) does not have significant effects on the phase assemblages formed across both classes of fly ashes. However, higher abundances lead to substantial modifications, as observed elsewhere.[3,59] More specifically, for the Class C fly ash in NaCl system, ionic strengths above 0.1 mol/L inhibit monosulfoaluminate, katoite, strätlingite and hydrotalcite formation (see Figure 1a). These phases are replaced by Cl-AFm phases. Friedel's salt forms for ionic strengths greater than 0.5 mol/L in NaCl system. For $CaCl_2$, ionic strengths above 0.3 mol/L similarly inhibit monosulfoaluminate, katoite and hydrotalcite formation (Figure 1b). The co-formation/-persistence of Kuzel's salt and Friedel's salt is observed in the ionic strength range of 1.5-3 mol/L, while Friedel's salt is the main hydrate formed, alongside a minority of ettringite for ionic strengths greater than 3 mol/L ($CaCl_2$).

Although no crystalline C-S-H phases were observed, the presence of amorphous C-S-H (i.e., generally with Ca/Si < 1.45)[60–62] is expected because of the pozzolanic reaction between the fly ashes and portlandite.

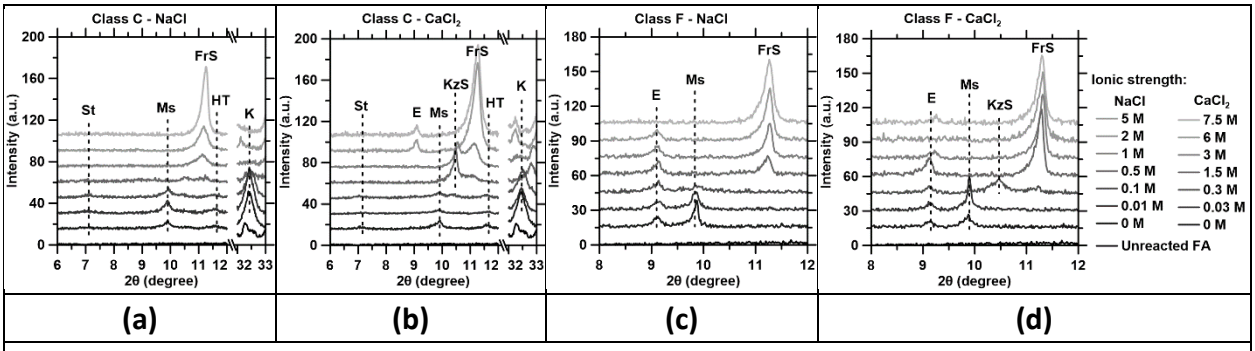

(a)	(b)	(c)	(d)

Figure 1. X-ray diffractograms for the Class C fly ash system in: **(a)** NaCl and **(b)** $CaCl_2$ solutions, and the Class F fly ash system in: **(c)** NaCl and **(d)** $CaCl_2$ solutions. Here, E = ettringite, Ms = monosulfoaluminate, FrS = Friedel's salt, KzS = Kuzel's salt, HT = hydrotalcite, St = strätlingite and K = katoite ($Ca_3Al_2(SiO_4)_{3-x}(OH)_{4x}$ with x = 1.5-3). For the unreacted Class C fly ash, the peaks at 31.25° and 32.6° 2θ are attributed to CaO and $MgCO_3$, respectively.

For the Class F fly ash in NaCl system, high ionic strengths (I_m > 0.1 mol/L) suppress monosulfoaluminate formation, while the formation of ettringite too is noted to be suppressed at ionic strengths of 5 mol/L. The formation of Friedel's salt (11.20° 2θ) is favored as sulfate is replaced by chloride as the interstitial anion within the AFm interlayer. In $CaCl_2$ system, ionic strengths above 0.03 mol/L prevent monosulfoaluminate formation, and ettringite's formation is inhibited at ionic strengths above 3 mol/L. Kuzel's salt formation (9.89° 2θ) is observed between 0.03 mol/L < I_m < 0.3 mol/L, while only Friedel's salt formation is observed at ionic strengths higher than 0.3 mol/L due to higher quantity of solubilized Ca^{2+} and Cl^- available in solution.

ATR-FTIR was used to ascertain the presence of amorphous hydrated phases. The presence of amorphous C-S-H was detected across both fly ash compositions after 10 days (peak between 950 and 965 cm^{-1}, Figure 2a and Figure S2). The position and shape of the peak is similar to that of Al-containing C-S-H as previously identified by Kapeluszna, et *al*.[61] While it is possible that the amorphous C-S-H formed may transform into variants of increasing crystallinity – in time, particularly at somewhat elevated curing temperatures – no crystalline C-S-H phases were detected over the course of the examinations carried out herein. In general, the C-S-H formed in the presence of NaCl brines shows a peak position and a peak intensity that is unaffected by NaCl concentration (Figure 2b and c). This suggests, to the first order, that there is no structural incorporation of Na^+ or Cl^- into the C-S-H, and that, rather, Na^+ and Cl^- interact with the C-S-H via physical (sorption) processes.[14–16] In contrast, the C-S-H peak intensity decreases with increasing $CaCl_2$ concentrations, while the peak position shifts to higher wavenumbers (for both Class C and Class F fly ashes), with the emergence of a second peak around 1015 cm^{-1} (Class F fly ash only). Both Ca/Si and Al/Si ratios of the C-(A)-S-H phases can influence the infrared peak position. In particular, an increasing Ca/Si ratio and decreasing Al/Si ratio of C-(A)-S-H have both

been shown to shift the peak position to higher wavenumbers.[61] Both of these compositional alterations can also result in the formation of a second peak around 1000 cm^{-1}.[61] As such, first, it is indicated that the shift in the peak position in the $CaCl_2$ system is linked to enhanced Cl-AFm phase formation that consumes mobile Al present in the system; resulting in a decrease of the Al/Si ratio. Second, an increasing $CaCl_2$ concentration provides additional calcium, which likely results in an increase of the Ca/Si ratio. The indications suggest that both an increase in Ca/Si and decrease in Al/Si ratios play a role in altering the peak position in the $CaCl_2$-brine systems. Additionally, increasing Cl-AFm formation in the $CaCl_2$ system likely consumes the C-(A)-S-H, as attested by the peak intensity decrease that is observed experimentally. Herein, Cl-AFm formation results in the decomposition of C-(A)-S-H into portlandite and amorphous silica, the former of which serves as a reactant in Cl-AFm formation.

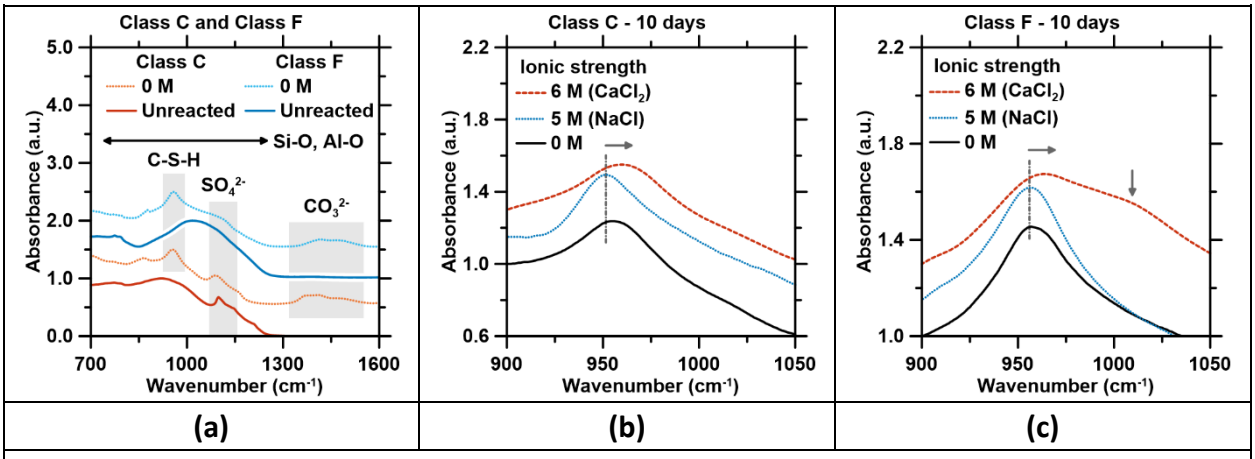

Figure 2. IR spectra of **(a)** unreacted and reacted (10 days hydration at 50 °C in DIW) Class C and Class F fly ash. **(b)** A zoomed-in view of the peak attributed to C-S-H for the Class C and **(c)** the Class F fly ash reacted in NaCl or $CaCl_2$ brines (the full FTIR spectra are shown in Figure S2).

Heat release and Cl-AFm formation: The degree of fly ash reaction is difficult to establish quantitatively. While several methods exist to assess the degree of reaction of fly ash, including selective dissolution,[63–65] SEM-image analysis,[26,64,66] etc., these methods present considerable uncertainty and/or are time-consuming.[64] First, it is instructive to assess how the cumulative heat release measured until 10 days is affected by brine composition (see Figure 3a). In general, a substantial effect of NaCl and $CaCl_2$ on fly ash reactivity is noted. The effect of both salts is minimal for ionic strengths below 0.3 mol/L across both fly ash types, which is consistent with the XRD data that showed little-to-no changes in phase assemblages in this ionic strength range. In contrast, for ionic strengths in excess of 0.3 mol/L, NaCl strongly suppresses the reactivity of Class C fly ash, while the reactivity of Class F fly is even somewhat enhanced; the latter, particularly for ionic strength in excess of 1 mol/L. On the other hand, while $CaCl_2$ slightly elevates Class F fly ash reactivity, the Class C fly ash's reactivity is initially suppressed and recovers for ionic strengths only in excess of 1.5 mol/L. This may indicate that reductions in water activity resulting from the presence of salts prominently affect Ca-based compounds which are more prevalent in the Class C fly ash as compared to Class F variants. However, the non-monotonous trend in heat release wherein the reactivity of Class C (and to a smaller

extent, Class F) fly ash appears to elevate for ionic strengths greater than 1 mol/L (Class C) and greater than 0.3 mol/L (Class F) remains unclear currently.

The mass loss from the Cl-AFm phases derived from thermal analysis (i.e., as measured between 250-and-430 °C, see Figure S3) shows that, expectedly, the amount of Cl-AFm formation increases with the Cl-content of the brine (see Figure 3b). The formation of Cl-AFm phases is particularly pronounced for ionic strengths greater than 0.1 mol/L. Across both fly ashes, a higher Cl-AFm content is observed in the case of $CaCl_2$-based brines, as compared to their NaCl counterparts on account of the provision of mobile Ca-species in the former. Interestingly, when the mass loss from thermal analysis corresponding to the Cl-AFm compounds is mapped as a function of the cumulative heat release, a "V-shape" – like the heat release behavior (see Figure 3a) – is observed in the case of the Class C fly ash (Figure 3c), while a linear trend emerges in the case of the Class F fly ash (Figure 3d). The correlation between the heat release and Cl-AFm phase abundance indicates that, broadly speaking, the formation of (one or more) Cl-AFm phases is a dominant reaction in fly ash-brine systems. Cl-AFm formation is beneficial to Class F fly ash reactivity, as it occurs in addition (i.e., not at the expense of) to ettringite formation. In contrast, Cl-AFm formation is detrimental to Class C fly ash reactivity, since it occurs at the expense of strätlingite, monosulfoaluminate and katoite; which are observed to be destabilized in the NaCl (I_m > 0.5 mol/L) and $CaCl_2$ (I_m > 0.3 mol/L) containing systems.

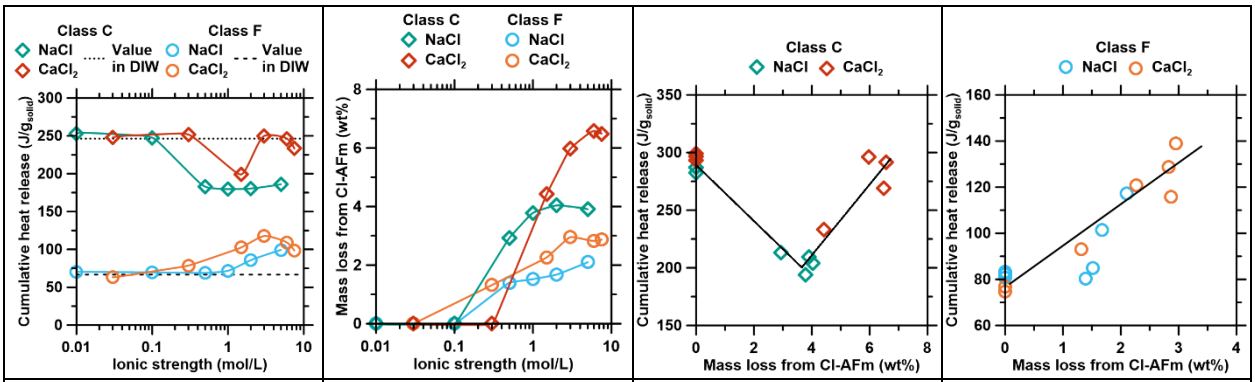

(a) **(b)** **(c)** **(d)**

Figure 3. (a) Cumulative heat release after 10 days of hydration at 50 °C as a function of the ionic strength. **(b)** Mass loss from Cl-AFm phases – measured between ~250 and ~430 °C – as a function of the ionic strength. The cumulative heat release after 10 days as a function of the mass loss from Cl-AFm phases for the: **(c)** Class C fly ash, and **(d)** Class F fly ash.

Thermodynamic modeling: Thermodynamic modeling based on the minimization of Gibbs free energies was used to estimate the stable phase assemblages that exist as a function of fly ash reactivity. Herein, the heterogeneity of the fly ash is taken into account, unlike most studies that considered the congruent dissolution of fly ash content based on its average composition as determined from XRF.[9] Thus, the crystalline phases that feature widely varying reactivities are programmed to dissolve following the observations of the short-term dissolution analysis. Based on this analysis, while quartz for example is assessed to be non-reactive, anhydrite

($CaSO_4$, i.e., present in both Class C and Class F fly ash) is assumed to rapidly react and be consumed. The amorphous phase dissolves congruently in relation to its average composition (shown in Table 3) following a linear dissolution expression from 0 to 100 mass %.

A key question here is related to estimating the degree of fly ash reaction following 10 days of hydration at 50 °C. The degree of fly ash reaction was inferred by analyzing when the ratio of masses of a single well-characterized crystalline phase, e.g., portlandite (CH: $Ca(OH)_2$) is equal to unity; i.e., when the modeled quantity of a given phase is equivalent to its content established by experimental, i.e., TGA and/or XRD assessments (e.g., when $CH_m/CH_e \approx 1$, where the subscripts 'm' and 'e' indicate modeled and experimental assessments). While it does not have any implications on the assessed degree of fly ash reaction, it should be noted that, expectedly, the quantity of amorphous C-S-H formed could not be determined experimentally and was thus considered part of the amorphous compounds as calculated by XRD analysis. For example, Figure 4(a-b) shows the modelled phase assemblage obtained in DIW for the Class C and the Class F fly ash, respectively, as a function of the fly ash degree of reaction. The red dashed lines indicate the degree of fly ash reaction for which the condition $CH_m/CH_e \approx 1$ is satisfied for the crystalline phase of interest; herein, portlandite.

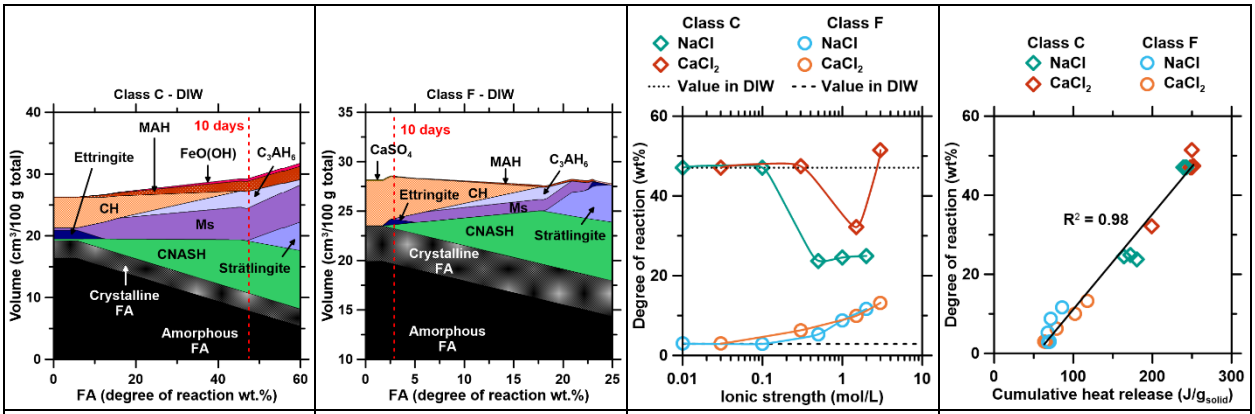

(a)	(b)	(c)	(d)

Figure 4. Thermodynamic modelling of **(a)** a Class C and **(b)** a Class F fly ash hydration in DIW in presence of $Ca(OH)_2$. Dashed red lines indicate the degree of reaction for which the best agreement is found between simulations and experiments phase quantity (on a mass bases). CH = portlandite, Ms = monosulfoaluminate, C_2AH_6 = katoite, CNASH = sodium substituted calcium aluminum silicate gel, MAH = hydroxyl hydrotalcite. **(c)** Fly ash degree of reaction as a function of ionic strength. **(d)** Comparison between the fly ash degree of reaction modelled and the experimental cumulative heat release.

Interestingly, it is noted that while the modeled phase assemblage of the Class F fly ash in DIW shows very good agreement with experimental data, comparatively, the Class C fly ash is not as well modeled. Particularly, in the case of the modeled Class C fly ash system (in DIW), the katoite content is underestimated, and the monosulfoaluminate content overestimated. This may suggest that the dissolution of the amorphous phase in the Class C fly ash may be incongruent, a not unexpected consideration, given the substantial Ca-content therein. In spite

of these differences, in general, reasonable agreement in the modeled and experimental phase relation is observed for both Class C and Class F fly ashes up to I_m = 2 mol/L (NaCl) and 3 mol/L ($CaCl_2$). The degree of reaction of the Class F fly ash increases with increasing ionic strength regardless of the type of salt considered (Figure 4c). On the other hand, the degree of reaction of the Class C fly ash decreases at I_m = 0.5 mol/L for NaCl and remains unchanged with increasing ionic strength. In contrast, the degree of reaction of the Class C fly ash decreases at I_m = 1.5 mol/L for $CaCl_2$ brines and increases thereafter with at higher ionic strengths. These observations are consistent with the cumulative heat release, and a good correlation is observed between the inferred degree of fly ash reaction and the cumulative heat release (see Figure 4d).

Effect of brine concentration on hydrate formation: An important experimental observation in the case of the NaCl and $CaCl_2$ brines is that, despite presenting similar initial Cl^- concentrations, the phase assemblages formed vary considerably, even for a single fly ash across the two brine compositions (see Figure 1). This implicates the role of the counterion. Interestingly, the GEMS modeling indicates that the pore solution pH observed in the NaCl brine is consistently higher than that of the $CaCl_2$ brine, for both Class C and Class F fly ashes (Figure 5); in some cases, up to 1 pH unit. Of note, while Cl^- species are consumed from both brines to form the Cl-AFm compounds, little if any Na^+ is taken up into the solids, other than Na^+ that may be sorbed by, or incorporated into C(-N)-A-S-H.[67,68] Expectedly, the consumed Cl^- ions are compensated by OH^- that forms, e.g., via the dissociation of water to ensure charge neutrality, resulting in a pH increase as has been observed previously in seawater systems.[59] In contrast, Ca^{2+} is consumed from the solution to form C(-N)-A-S-H, AFm phases, and conceivably portlandite; whereby the consumption of Ca^{2+} is compensated by an increase in the acidity ([H^+] abundance) of the solution resulting in a decrease of pH.

Since the stability of numerous cementitious phases is sensitively linked to the solution pH (e.g., ettringite and AFm), the solution pH variations begin to explain why different phase assemblages are observed (see Supplementary Information: Figure S4),[69–72] in NaCl and $CaCl_2$-based brines. It is furthermore noted that the simulated pH for each of the brine systems varies considerably across different ionic strengths (Figure 5). Although the pore solution chemistry and pH were not specifically analyzed herein, previous studies have shown favorable agreement between measured and modeled pore solution attributes.[30,73,74] As a result of the variation in pH, for Class F fly ashes, the differences in pH alter the quantity of ettringite formed, as in Cl-containing solutions, ettringite stability decreases with increasing pH, and no ettringite formation is observed above a pH of 12.5 (see Supplementary Information: Figure S4). This is, however, only valid for Cl^- concentrations greater than 0.1 M as ettringite is known to be stable at pH > 13 in DIW and in dilute Cl^- solutions. In the case of the Class C fly ash in the $CaCl_2$ system, the pH remains in a range that allows ettringite formation. In the NaCl system however, the pH approaches the limits of stability for Kuzel's and Friedel's salts since for pH > 13.5, both Cl-AFms are replaced by katoite (see Supplementary Information: Figure S4) although the kinetics of this transformation are likely affected by the particular chemistry of the pore solution.

All systems modelled here show differences in Cl^--binding efficiency (see Supplementary Information: Figure S5), resulting from the differences in the reactant (i.e., brine and fly ash) compositions which dictate the amount and stability of phases formed. Importantly, since the relationship between the chloride concentration of the brine and the amount of Cl-AFm formed is not fully linear (Figure 3b); the Cl^--binding (i.e., ability to retain Cl^- species within hydrated phases) varies accordingly (see Figure S5). Class F fly ash systems, in particular, cannot retain more than 40% of the mobile Cl^- content, regardless of the type (Na, Ca) of brine. On the other hand, while Class C fly ash shows a reduced efficiency to retain mobile Cl^- at high ionic strengths it can achieve monotonically increasing Cl^--binding with $CaCl_2$ up to 88%; even for the highest ionic strengths considered. These results highlight the need for incorporating cost-effective additives that offer mobile Ca, and Al (i.e., to favor Cl-AFm formation) to maximize Cl^- encapsulation across a diversity of brine and fly ash compositions.

Additional considerations: The results herein indicate that there are two key attributes that are vital for accurate thermodynamic modeling of brine encapsulation/S&S including:

- Compositional heterogeneity of the fly ash, and,
- The effects of brine composition and concentration (ionic strength) on fly ash reactivity.

Foremost, it is inaccurate to consider congruent dissolution of the bulk fly ashes. Rather, it is necessary to consider the distinguished reactivities of the crystalline and amorphous phases and make use of dissolution assessments to establish which phases may be considered readily reactive (i.e., similar or higher reactivity as the fly ash's glass), or not. SEM analysis of Class F fly ashes has previously showed that the amorphous content is relatively homogenous,[25,26,28,75] and that the dissolution rate of its main components are similar.[26] This implies that assuming congruent dissolution of its amorphous phase is reasonable. Surprisingly, thermodynamic modeling of a Class C fly ash was unable to replicate experimental phase balances as accurately when its amorphous phase was assumed to react (dissolve) congruently. This may indicate that it is necessary to consider the dissolution rates of its major glass components discretely, or establish an incongruent dissolution expression for the average glass composition.[26,29] It is further observed that the brine composition markedly affects fly ash reactivity. Some changes in fly ash reactivity, particularly of Class C fly ashes, are indeed attributable to water activity reductions.[44,76,77] Other aspects, perhaps including the stability of the different Cl-AFm phases, and the implications of the persisting solution pH and composition, are required to understand the nature and kinetics of phase transformations that may result in Ca- and Na-brine systems as a function of time, ambient temperature, and moisture conditions (i.e., relative humidity, RH).

Coming back to considerations of temperature, and reaction consideration, Han, *et al*.[41] studied the pozzolanic reactions of Class F fly ashes in water at various temperatures and suggested an apparent activation energy of fly ash reactions in the range of 43-50 kJ/mol. This is in agreement with the data of Bentz[42] across a variety of systems (35-50 kJ/mol). These values are, however, much lower than that expected for CAS [CaO-Al_2O_3-SiO_2] glass dissolution (70-90 kJ/mol for nuclear glasses,[78] 102 kJ/mol for two class F fly ashes in hyperalkaline solutions[79]). This may suggest that, in brine encapsulation applications, glass dissolution is transport-controlled due to the fast early-precipitation of the hydrated phases. It should be noted that, in

brine encapsulation, aging occurs over a period of several months. As such, the systems considered herein may still be somewhat "immature" and may be expected to show ongoing evolutions in phase balances, in time. Unsurprisingly, despite the presence of sufficient $Ca(OH)_2$, Class F fly ash reactivity remains low (<15 mass % after 10 days at 50 °C). In contrast, Class C fly ash reacts more substantially (up to 50 mass % after 10 days at 50 °C), but its reactivity is strongly inhibited at high-NaCl concentrations – likely due to water activity considerations – although much less so in $CaCl_2$-based brines. It should also be noted that while the GEMS simulations indicate that the pozzolanic reaction of Class C and Class F fly ashes with portlandite results in the formation of C-(N)-A-S-H compounds, this may not be the main driving reaction. In fact, both our isothermal calorimetry and TGA data suggest that the formation of Cl-AFm phases is the major contributor to Cl-uptake (and chemical reaction) in these systems.

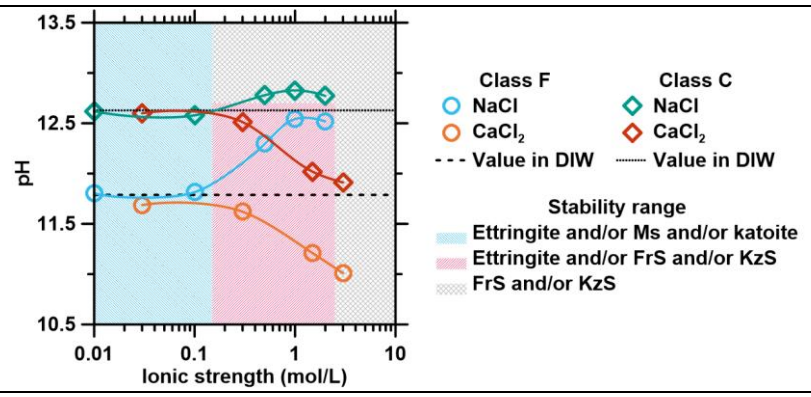

Figure 5. A comparison of the (pore) solution pH after 10 days of hydration at 50 °C (i.e. for the degree of fly ash reaction shown in Figure 4c) as a function of the solvent chemistry (DIW, $CaCl_2$ or NaCl) for Class C and Class F fly ash systems as calculated by GEMS modeling.

Nevertheless, taken together, the approach shown here demonstrates how GEMS-type geochemical simulations can be used to rapidly design and screen formulations for S&S applications, with due considerations of chemical attributes, e.g., pH, brine composition, fly ash composition, etc. and the implications on wastewater, and ion-encapsulation consumption. This is important to identify the optimal combinations of brine and fly ash, and to also assess if additives may be needed, e.g., cement, lime, etc. to enhance S&S performance. This work also shows a means to assess the differences in pore solution pH that may result in different formulations, since it is sought to maintain a pH > 13 to ensure that heavy metals precipitate as insoluble species.[5,6] While this work has focused on Na, Ca-based chloride brine compositions, in reality, the range of possibly compositions is much broader. For example, not only can brines contain species other than Na, Ca, and Cl, but more broadly, water treatment systems may also produce sulfate-rich brines including those based on magnesium compositions. While consideration of each of these aspects is beyond the scope of this paper, the general approach elaborated herein can be used to study the interactions and compatibility of diverse brine and fly ash types and compositions. This is significant as opportunities exist for knowledge of the nature developed herein to influence the selection of upstream treatment technology options such as reverse osmosis or thermal evaporation such that an optimal brine concentration can

be achieved and matched to the coal-combustion residuals produced over the course of electricity production operations.

SUMMARY AND CONCLUSIONS

This paper has shown that the brine composition (NaCl or $CaCl_2$) and its ionic strength ($0 \leq I_m \leq 7.5$ mol/L) strongly affect: (1) the phase assemblage formed, and (2) the fly ash degree of reaction. In general, hypersaline NaCl and $CaCl_2$ brines strongly promote the formation of Cl-AFm phases including: Friedel's and/or Kuzel's salts. The formation of the Cl-AFm phases, however, is counterbalanced by the destabilization of other phases that are otherwise stable in DI-water (e.g. katoite, strätlingite, monosulfoaluminate, etc.) with increasing chloride abundance. Thermodynamic modeling indicates that such phase stability is related to differences in the prevailing pH: e.g., a strong increase in pH is observed in NaCl systems with increasing Cl^- consumption. In contrast, Ca^{2+} is consumed alongside Cl^- to form hydrated phases in a $CaCl_2$ system, and the pH consequently decreases. These differences in pH, and phase stability as a function of brine composition and ionic strength also result in differences in the reactivity of Class C and Class F fly ashes, wherein the reactivity of the Class C fly ashes is furthermore affected by reductions in the water activity with increasing brine salinity. Taken together, the outcomes of this work illustrate the need to select the appropriate combination of fly ash type and additive to match brine composition, to ensure effective S&S. This information is important as it enhances our ability, *a priori*, to rapidly screen S&S compositions as a function of practical considerations including: (desired) extent of water volume reduction, Cl^-, and/or SO_4^{2-} consumption, the prevailing pH of the pore solution, etc. Amongst others, such information forms a critical input to reactive-transport calculations which seek to assess the performance and contaminant retention ability of encapsulation materials and S&S operations.

ACKNOWLEDGMENTS

The authors acknowledge financial support for this research provided by the Electric Power Research Institute (EPRI) and the Department of Energy via the Advanced Research Projects Agency-Energy (ARPA-e: DE-AR-0001147). The contents of this paper reflect the views and opinions of the authors, who are responsible for the accuracy of data presented herein. This research was conducted in the Laboratory for the Chemistry of Construction Materials (LC^2) and the Molecular Instrumentation Center (MIC) at the University of California, Los Angeles (UCLA). As such, the authors acknowledge the support that has made these laboratories and their operations possible.

SUPPORTING INFORMATION

Additional isothermal calorimetry data (Figure S1), IR spectroscopy data (Figure S2), TGA data (Figure S3), and equilibrium diagram of ettringite and monosulfoaluminate as a function of pH and Cl concentration (Figure S4).

REFERENCES

(1) U.S. EPA (Environmental Protection Agency). *Effluent Limitations Guidelines and Standards for the Steam Electric Power Generating Point Source Category*; 2015–25663; 2015; p 67.

(2) U.S. EPA (Environmental Protection Agency). *Annual Effluent Guidelines Review Report*; 821-R-14–004; 2012; p 276.

(3) Renew, J. E.; Huang, C.-H.; Burns, S. E.; Carrasquillo, M.; Sun, W.; Ellison, K. M. Immobilization of Heavy Metals by Solidification/Stabilization of Co-Disposed Flue Gas Desulfurization Brine and Coal Fly Ash. *Energy Fuels* **2016**, *30* (6), 5042–5051. https://doi.org/10.1021/acs.energyfuels.6b00321.

(4) Huang, C.-H.; Renew, J. E.; Wenlong Zhang, M. S. *Mineralogy Optimization for Metal and Chloride Immobilization in Co-Disposed Flue Gas Desulfurization Brines and Bituminous Coal Fly Ash*; 2019; p 42.

(5) Glasser, F. P. Fundamental Aspects of Cement Solidification and Stabilisation. *J. Hazard. Mater.* **1997**, *52* (2–3), 151–170. https://doi.org/10.1016/S0304-3894(96)01805-5.

(6) Van Jaarsveld, J. G. S.; Van Deventer, J. S. J.; Lorenzen, L. The Potential Use of Geopolymeric Materials to Immobilise Toxic Metals: Part I. Theory and Applications. *Miner. Eng.* **1997**, *10* (7), 659–669. https://doi.org/10.1016/S0892-6875(97)00046-0.

(7) Gougar, M. L. D.; Scheetz, B. E.; Roy, D. M. Ettringite and C-S-H Portland Cement Phases for Waste Ion Immobilization: A Review. *Waste Manag.* **1996**, *16* (4), 295–303. https://doi.org/10.1016/S0956-053X(96)00072-4.

(8) Piekkari, K.; Ohenoja, K.; Isteri, V.; Tanskanen, P.; Illikainen, M. Immobilization of Heavy Metals, Selenate, and Sulfate from a Hazardous Industrial Side Stream by Using Calcium Sulfoaluminate-Belite Cement. *J. Clean. Prod.* **2020**, *258*, 120560. https://doi.org/10.1016/j.jclepro.2020.120560.

(9) Okoronkwo, M. U.; Balonis, M.; Katz, L.; Juenger, M.; Sant, G. A Thermodynamics-Based Approach for Examining the Suitability of Cementitious Formulations for Solidifying and Stabilizing Coal-Combustion Wastes. *J. Environ. Manage.* **2018**, *217*, 278–287. https://doi.org/10.1016/j.jenvman.2018.02.095.

(10) Kogbara, R. B.; Al-Tabbaa, A.; Stegemann, J. A. Comparisons of Operating Envelopes for Contaminated Soil Stabilised/Solidified with Different Cementitious Binders. *Environ. Sci. Pollut. Res.* **2014**, *21* (5), 3395–3414. https://doi.org/10.1007/s11356-013-2276-7.

(11) Song, Y.; Yang, K.; Chen, J.; Wang, K.; Sant, G.; Bauchy, M. Machine Learning Enables Rapid Screening of Reactive Fly Ashes Based on Their Network Topology. *ACS Sustain. Chem. Eng.* **2021**, *9* (7), 2639–2650. https://doi.org/10.1021/acssuschemeng.0c06978.

(12) U.S. EPA (Environmental Protection Agency). *Waste and Materials - Flow Benchmark Sector Report: Beneficial Use of Secondary Materials - Coal Combustion Products*; 2008; p 95.

(13) Ellison, K. Brine-Encapsulation Bench & Field Testing Recommendations; Lexington, KY, 2017.

(14) Hirao, H.; Yamada, K.; Takahashi, H.; Zibara, H. Chloride Binding of Cement Estimated by Binding Isotherms of Hydrates. *J. Adv. Concr. Technol.* **2005**, *3* (1), 77–84. https://doi.org/10.3151/jact.3.77.

(15) Gégout, P.; Revertégat, E.; Moine, G. Action of Chloride Ions on Hydrated Cement Pastes: Influence of the Cement Type and Long Time Effect of the Concentration of Chlorides. *Cem. Concr. Res.* **1992**, *22* (2–3), 451–457. https://doi.org/10.1016/0008-8846(92)90088-D.

(16) Beaudoin, J. J.; Ramachandran, V. S.; Feldman, R. F. Interaction of Chloride and C-S-H. *Cem. Concr. Res.* **1990**, *20* (6), 875–883. https://doi.org/10.1016/0008-8846(90)90049-4.

(17) Balonis, M.; Lothenbach, B.; Le Saout, G.; Glasser, F. P. Impact of Chloride on the Mineralogy of Hydrated Portland Cement Systems. *Cem. Concr. Res.* **2010**, *40* (7), 1009–1022. https://doi.org/10.1016/j.cemconres.2010.03.002.

(18) Mesbah, A.; François, M.; Cau-dit-Coumes, C.; Frizon, F.; Filinchuk, Y.; Leroux, F.; Ravaux, J.; Renaudin, G. Crystal Structure of Kuzel's Salt $3CaO{\cdot}Al_2O_3{\cdot}1/2CaSO_4{\cdot}1/2CaCl_2{\cdot}11H_2O$ Determined by Synchrotron Powder Diffraction. *Cem. Concr. Res.* **2011**, *41* (5), 504–509. https://doi.org/10.1016/j.cemconres.2011.01.015.

(19) Jeon, D.; Yum, W. S.; Jeong, Y.; Oh, J. E. Properties of Quicklime (CaO)-Activated Class F Fly Ash with the Use of $CaCl_2$. *Cem. Concr. Res.* **2018**, *111*, 147–156. https://doi.org/10.1016/j.cemconres.2018.05.019.

(20) Glasser, F. P.; Kindness, A.; Stronach, S. A. Stability and Solubility Relationships in AFm Phases Part I. Chloride, Sulfate and Hydroxide. *Cem. Concr. Res.* **1999**, *29* (6), 861–866. https://doi.org/10.1016/S0008-8846(99)00055-1.

(21) Birnin-Yauri, U. A.; Glasser, F. P. Friedel's Salt, $Ca_2Al(OH)_6(Cl,OH){\cdot}2H_2O$: Its Solid Solutions and Their Role in Chloride Binding. *Cem. Concr. Res.* **1998**, *28* (12), 1713–1723. https://doi.org/10.1016/S0008-8846(98)00162-8.

(22) Qiao, C.; Suraneni, P.; Weiss, J. Damage in Cement Pastes Exposed to NaCl Solutions. *Constr. Build. Mater.* **2018**, *171*, 120–127. https://doi.org/10.1016/j.conbuildmat.2018.03.123.

(23) Jones, C.; Ramanathan, S.; Suraneni, P.; Hale, W. M. Calcium Oxychloride: A Critical Review of the Literature Surrounding the Formation, Deterioration, Testing Procedures, and Recommended Mitigation Techniques. *Cem. Concr. Compos.* **2020**, *113*, 103663. https://doi.org/10.1016/j.cemconcomp.2020.103663.

(24) Peterson, K.; Julio-Betancourt, G.; Sutter, L.; Hooton, R. D.; Johnston, D. Observations of Chloride Ingress and Calcium Oxychloride Formation in Laboratory Concrete and Mortar at 5 °C. *Cem. Concr. Res.* **2013**, *45*, 79–90. https://doi.org/10.1016/j.cemconres.2013.01.001.

(25) Chancey, R. T.; Stutzman, P.; Juenger, M. C. G.; Fowler, D. W. Comprehensive Phase Characterization of Crystalline and Amorphous Phases of a Class F Fly Ash. *Cem. Concr. Res.* **2010**, *40* (1), 146–156. https://doi.org/10.1016/j.cemconres.2009.08.029.

(26) Durdziński, P. T.; Dunant, C. F.; Haha, M. B.; Scrivener, K. L. A New Quantification Method Based on SEM-EDS to Assess Fly Ash Composition and Study the Reaction of Its Individual Components in Hydrating Cement Paste. *Cem. Concr. Res.* **2015**, *73*, 111–122. https://doi.org/10.1016/j.cemconres.2015.02.008.

(27) Durdziński, P. T.; Snellings, R.; Dunant, C. F.; Haha, M. B.; Scrivener, K. L. Fly Ash as an Assemblage of Model Ca–Mg–Na-Aluminosilicate Glasses. *Cem. Concr. Res.* **2015**, *78*, 263–272. https://doi.org/10.1016/j.cemconres.2015.08.005.

(28) Oey, T.; Timmons, J.; Stutzman, P.; Bullard, J. W.; Balonis, M.; Bauchy, M.; Sant, G. An Improved Basis for Characterizing the Suitability of Fly Ash as a Cement Replacement Agent. *J. Am. Ceram. Soc.* **2017**, *100* (10), 4785–4800. https://doi.org/10.1111/jace.14974.

(29) Glosser, D.; Suraneni, P.; Isgor, O. B.; Weiss, W. J. Estimating Reaction Kinetics of Cementitious Pastes Containing Fly Ash. *Cem. Concr. Compos.* **2020**, *112*, 103655. https://doi.org/10.1016/j.cemconcomp.2020.103655.

(30) Lothenbach, B.; Winnefeld, F. Thermodynamic Modelling of the Hydration of Portland Cement. *Cem. Concr. Res.* **2006**, *36* (2), 209–226. https://doi.org/10.1016/j.cemconres.2005.03.001.

(31) Dove, P. M. The Dissolution Kinetics of Quartz in Aqueous Mixed Cation Solutions. *Geochim. Cosmochim. Acta* **1999**, *63* (22), 3715–3727. https://doi.org/10.1016/S0016-7037(99)00218-5.

(32) Dove, P. M.; Elston, S. F. Dissolution Kinetics of Quartz in Sodium Chloride Solutions: Analysis of Existing Data and a Rate Model for 25 °C. *Geochim. Cosmochim. Acta* **1992**, *56* (12), 4147–4156. https://doi.org/10.1016/0016-7037(92)90257-J.

(33) Dove, P. M.; Nix, C. J. The Influence of the Alkaline Earth Cations, Magnesium, Calcium, and Barium on the Dissolution Kinetics of Quartz. *Geochim. Cosmochim. Acta* **1997**, *61* (16), 3329–3340. https://doi.org/10.1016/S0016-7037(97)00217-2.

(34) Jollivet, P.; Frugier, P.; Parisot, G.; Mestre, J. P.; Brackx, E.; Gin, S. Effect of Clayey Groundwater on the Dissolution Rate of the Simulated Nuclear Waste Glass SON68. *J. Nucl. Mater.* **2012**, *420* (1–3), 508–518. https://doi.org/10.1016/j.jnucmat.2011.10.026.

(35) Wickert, C. L.; Vieira, A. E.; Dehne, J. A.; Wang, X.; Wilder, D. M.; Barkatt, A. Effects of Salts on Silicate Glass Dissolution in Water: Kinetics and Mechanisms of Dissolution and Surface Cracking. *Phys. Chem. Glas.* **1999**, *40* (3), 157–170.

(36) La Plante, E. C.; Oey, T.; Hsiao, Y.-H.; Perry, L.; Bullard, J. W.; Sant, G. Enhancing Silicate Dissolution Kinetics in Hyperalkaline Environments. *J. Phys. Chem. C* **2019**, *123* (6), 3687–3695. https://doi.org/10.1021/acs.jpcc.8b12076.

(37) Nishida, T.; Otsuki, N.; Ohara, H.; Garba-Say, Z. M.; Nagata, T. Some Considerations for Applicability of Seawater as Mixing Water in Concrete. *J. Mater. Civ. Eng.* **2015**, *27* (7). https://doi.org/10.1061/(ASCE)MT.1943-5533.0001006.

(38) Rietveld, H. M. A Profile Refinement Method for Nuclear and Magnetic Structures. *J. Appl. Crystallogr.* **1969**, *2* (2), 65–71. https://doi.org/10.1107/S0021889869006558.

(39) Bergmann, J.; Friedel, P.; Kleeberg, R. BGMN - a New Fundamental Parameters Based Rietveld Program for Laboratory X-Ray Sources, It's Use in Quantitative Analysis and Structure Investigations. *Comm. Powder Diffr. IUCr* **1998**, *20*, 5–8.

(40) Doebelin, N.; Kleeberg, R. Profex: A Graphical User Interface for the Rietveld Refinement Program BGMN. *J. Appl. Crystallogr.* **2015**, *48* (5), 1573–1580. https://doi.org/10.1107/S1600576715014685.

(41) Han, F.; He, X.; Zhang, Z.; Liu, J. Hydration Heat of Slag or Fly Ash in the Composite Binder at Different Temperatures. *Thermochim. Acta* **2017**, *655*, 202–210. https://doi.org/10.1016/j.tca.2017.07.002.

(42) Bentz, D. P. Activation Energies of High-Volume Fly Ash Ternary Blends: Hydration and Setting. *Cem. Concr. Compos.* **2014**, *53*, 214–223. https://doi.org/10.1016/j.cemconcomp.2014.06.018.

(43) Suraneni, P.; Weiss, J. Examining the Pozzolanicity of Supplementary Cementitious Materials Using Isothermal Calorimetry and Thermogravimetric Analysis. *Cem. Concr. Compos.* **2017**, *83*, 273–278. https://doi.org/10.1016/j.cemconcomp.2017.07.009.

(44) Oey, T.; Kumar, A.; Falzone, G.; Huang, J.; Kennison, S.; Bauchy, M.; Neithalath, N.; Bullard, J. W.; Sant, G. The Influence of Water Activity on the Hydration Rate of Tricalcium Silicate. *J. Am. Ceram. Soc.* **2016**, *99* (7), 2481–2492. https://doi.org/10.1111/jace.14181.

(45) ASTM D4326-04. *Standard Test Method for Major and Minor Elements in Coal and Coke Ash by X-Ray Fluorescence*; ASTM International: West Conshohocken, PA, 2004.

(46) Lothenbach, B.; Durdziński, P. T.; De Weerdt, K. Thermogravimetric Analysis. In *A practical guide to Microstructural analysis of cementitious materials*; Boca Raton, 2016.

(47) Shi, Z.; Geiker, M. R.; Lothenbach, B.; De Weerdt, K.; Garzón, S. F.; Enemark-Rasmussen, K.; Skibsted, J. Friedel's Salt Profiles from Thermogravimetric Analysis and Thermodynamic Modelling of Portland Cement-Based Mortars Exposed to Sodium Chloride Solution. *Cem. Concr. Compos.* **2017**, *78*, 73–83. https://doi.org/10.1016/j.cemconcomp.2017.01.002.

(48) Kulik, D. A.; Wagner, T.; Dmytrieva, S. V.; Kosakowski, G.; Hingerl, F. F.; Chudnenko, K. V.; Berner, U. R. GEM-Selektor Geochemical Modeling Package: Revised Algorithm and GEMS3K Numerical Kernel for Coupled Simulation Codes. *Comput. Geosci.* **2012**. https://doi.org/10.1007/s10596-012-9310-6.

(49) Wagner, T.; Kulik, D. A.; Hingerl, F. F.; Dmytrieva, S. V. GEM-Selektor Geochemical Modeling Package: TSolMod Library and Data Interface for Multicomponent Phase Models. *Can. Mineral.* **2012**, *50* (5), 1173–1195. https://doi.org/10.3749/canmin.50.5.1173.

(50) Lothenbach, B.; Matschei, T.; Möschner, G.; Glasser, F. P. Thermodynamic Modelling of the Effect of Temperature on the Hydration and Porosity of Portland Cement. *Cem. Concr. Res.* **2008**, *38* (1), 1–18. https://doi.org/10.1016/j.cemconres.2007.08.017.

(51) Lothenbach, B.; Kulik, D. A.; Matschei, T.; Balonis, M.; Baquerizo, L.; Dilnesa, B.; Miron, G. D.; Myers, R. J. Cemdata18: A Chemical Thermodynamic Database for Hydrated Portland Cements and Alkali-Activated Materials. *Cem. Concr. Res.* **2019**, *115*, 472–506. https://doi.org/10.1016/j.cemconres.2018.04.018.

(52) Thoenen, T.; Hummel, W.; Berner, U.; Curti, E. *The PSINagra Chemical Thermodynamic Database 12/07*, Villigen PSI.; Switzerland, 2014.

(53) Johnson, J. W.; Oelkers, E. H.; Helgeson, H. C. SUPCRT92: A Software Package for Calculating the Standard Molal Thermodynamic Properties of Minerals, Gases, Aqueous Species, and Reactions from 1 to 5000 Bar and 0 to 1000 °C. *Comput. Geosci.* **1992**, *18* (7), 899–947. https://doi.org/10.1016/0098-3004(92)90029-Q.

(54) Hummel, W.; Berner, U.; Curti, E.; Pearson, F. J.; Thoenen, T. Nagra/PSI Chemical Thermodynamic Data Base 01/01. *Radiochim. Acta* **2002**, *90* (9–11). https://doi.org/10.1524/ract.2002.90.9-11_2002.805.

(55) Helgeson, H. C.; Kirkham, D. H.; Flowers, G. C. Theoretical Prediction of the Thermodynamic Behavior of Aqueous Electrolytes by High Pressures and Temperatures; IV, Calculation of Activity Coefficients, Osmotic Coefficients, and Apparent Molal and Standard and Relative Partial Molal Properties to 600 Degrees C and 5kb. *Am. J. Sci.* **1981**, *281* (10), 1249–1516. https://doi.org/10.2475/ajs.281.10.1249.

(56) Vollpracht, A.; Lothenbach, B.; Snellings, R.; Haufe, J. The Pore Solution of Blended Cements: A Review. *Mater. Struct.* **2016**, *49* (8), 3341–3367. https://doi.org/10.1617/s11527-015-0724-1.

(57) Pitzer, K. S. Ion Interaction Approach: Theory and Data Correlation. In *Activity Coefficients in Electrolyte Solutions*; CRC Press: Boca Raton, 1991; pp 75–153.

(58) Langmuir, D. *Aqueous Environmental Geochemistry*; 1998.

(59) Montanari, L.; Suraneni, P.; Tsui-Chang, M.; Khatibmasjedi, M.; Ebead, U.; Weiss, J.; Nanni, A. Hydration, Pore Solution, and Porosity of Cementitious Pastes Made with Seawater. *J. Mater. Civ. Eng.* **2019**, *31* (8), 04019154. https://doi.org/10.1061/(ASCE)MT.1943-5533.0002818.

(60) Lothenbach, B.; Nonat, A. Calcium Silicate Hydrates: Solid and Liquid Phase Composition. *Cem. Concr. Res.* **2015**, *78*, 57–70. https://doi.org/10.1016/j.cemconres.2015.03.019.

(61) Kapeluszna, E.; Kotwica, Ł.; Różycka, A.; Gołek, Ł. Incorporation of Al in C-A-S-H Gels with Various Ca/Si and Al/Si Ratio: Microstructural and Structural Characteristics with DTA/TG, XRD, FTIR and TEM Analysis. *Constr. Build. Mater.* **2017**, *155*, 643–653. https://doi.org/10.1016/j.conbuildmat.2017.08.091.

(62) Chen, J. J.; Thomas, J. J.; Taylor, H. F. W.; Jennings, H. M. Solubility and Structure of Calcium Silicate Hydrate. *Cem. Concr. Res.* **2004**, *34* (9), 1499–1519. https://doi.org/10.1016/j.cemconres.2004.04.034.

(63) Suprenant, B. A.; Papadopoulos, G. Selective Dissolution of Portland-fly-ash Cements. *J. Mater. Civ. Eng.* **1991**, *3* (1), 48–59. https://doi.org/10.1061/(ASCE)0899-1561(1991)3:1(48).

(64) Durdziński, P.; Ben Haha, M.; Bernal, S. A.; De Belie, N.; Gruyaert, E.; Lothenbach, B.; Menendez Mendez, E.; Provis, J. L.; Scholer, A.; Stabler, C.; Tan, Z.; Villagran Zaccardi, Y.; Vollpracht, A.; Winnefeld, F.; Zajac, M.; Scrivener, K. L. Outcomes of the RILEM Round Robin on Degree of Reaction of Slag and Fly Ash in Blended Cements. *Mater. Struct.* **2017**, *50*, 135. https://doi.org/10.1617/s11527-017-1002-1.

(65) Han, F.; Liu, J.; Yan, P. Comparative Study of Reaction Degree of Mineral Admixture by Selective Dissolution and Image Analysis. *Constr. Build. Mater.* **2016**, *114*, 946–955. https://doi.org/10.1016/j.conbuildmat.2016.03.221.

(66) Haha, M. B.; De Weerdt, K.; Lothenbach, B. Quantification of the Degree of Reaction of Fly Ash. *Cem. Concr. Res.* **2010**, *40* (11), 1620–1629. https://doi.org/10.1016/j.cemconres.2010.07.004.

(67) Hong, S.-Y.; Glasser, F. P. Alkali Sorption by C-S-H and C-A-S-H Gels Part II. Role of Alumina. *Cem. Concr. Res.* **2002**, *32* (7), 1101–1111. https://doi.org/10.1016/S0008-8846(02)00753-6.

(68) Hong, S.-Y.; Glasser, F. P. Alkali Binding in Cement Pastes Part I. The C-S-H Phase. *Cem. Concr. Res.* **1999**, *29* (12), 1893–1903. https://doi.org/10.1016/S0008-8846(99)00187-8.

(69) Feng, P.; Miao, C.; Bullard, J. W. Factors Influencing the Stability of AFm and AFt in the Ca-Al-S-O-H System at 25 °C. *J. Am. Ceram. Soc.* **2016**, *99* (3), 1031–1041. https://doi.org/10.1111/jace.13971.

(70) Damidot, D.; Glasser, F. P. Thermodynamic Investigation of the CaO-Al_2O_3-$CaSO_4$-K_2O-H_2O System at 25 °C. *Cem. Concr. Res.* **1993**, *23* (5), 1195–1204. https://doi.org/10.1016/0008-8846(93)90180-H.

(71) Damidot, D.; Stronach, S.; Kindness, A.; Atkins, M.; Glasser, F. P. Thermodynamic Investigation of the CaO-Al_2O_3-$CaCO_3$-H_2O Closed System at 25 °C and the Influence of Na_2O. **1994**, *24* (3), 563–572. https://doi.org/10.1016/0008-8846(94)90145-7.

(72) Matschei, T.; Lothenbach, B.; Glasser, F. P. The AFm Phase in Portland Cement. *Cem. Concr. Res.* **2007**, *37* (2), 118–130. https://doi.org/10.1016/j.cemconres.2006.10.010.

(73) Lothenbach, B.; Gruskovnjak, A. Hydration of Alkali-Activated Slag: Thermodynamic Modelling. *Adv. Cem. Res.* **2007**, *19* (2), 81–92. https://doi.org/10.1680/adcr.2007.19.2.81.

(74) Zuo, Y.; Nedeljković, M.; Ye, G. Coupled Thermodynamic Modelling and Experimental Study of Sodium Hydroxide Activated Slag. *Constr. Build. Mater.* **2018**, *188*, 262–279. https://doi.org/10.1016/j.conbuildmat.2018.08.087.

(75) Durdziński, P. T.; Ben Haha, M.; Zajac, M.; Scrivener, K. L. Phase Assemblage of Composite Cements. *Cem. Concr. Res.* **2017**, *99*, 172–182. https://doi.org/10.1016/j.cemconres.2017.05.009.

(76) Lapeyre, J.; Ma, H.; Okoronkwo, M.; Sant, G.; Kumar, A. Influence of Water Activity on Hydration of Tricalcium Aluminate-calcium Sulfate Systems. *J. Am. Ceram. Soc.* **2020**, *103* (6), 3851–3870. https://doi.org/10.1111/jace.17046.

(77) Cook, R.; Ma, H.; Okoronkwo, M.; Sant, G.; Kumar, A. Influence of Water Activity on Belite (B-C_2S) Hydration. *J. Am. Ceram. Soc.* **2021**, *104* (4), 1831–1840. https://doi.org/10.1111/jace.17608.

(78) Strachan, D. M. Glass Dissolution : Testing and Modeling for Long-Term Behavior. *J. Nucl. Mater.* **2001**, *298* (1–2), 69–77. https://doi.org/10.1016/S0022-3115(01)00572-4.

(79) Chen, C.; Gong, W.; Lutze, W.; Pegg, I. L.; Zhai, J. Kinetics of Fly Ash Leaching in Strongly Alkaline Solutions. *J. Mater. Sci.* **2010**, *46* (3), 590–597. https://doi.org/10.1007/s10853-010-4997-z.

TOC/ABSTRACT GRAPHIC

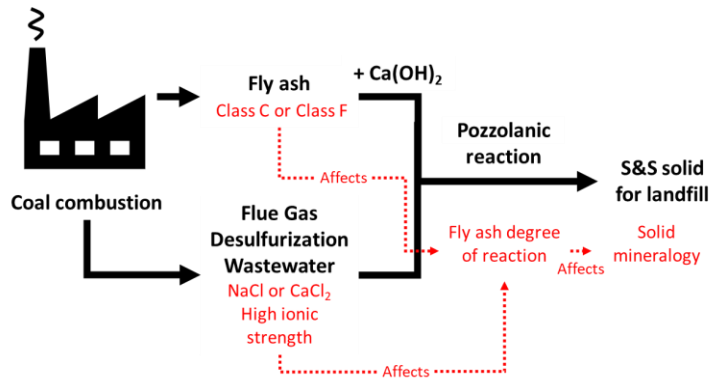

SYNOPSIS

This work increases our understanding of the interactions between hypersaline brines and the resulting cementitious matrix formed during solidification and stabilization processes.